JGR Space Physics

RESEARCH ARTICLE
10.1029/2019JA027089

Effects of Energetic Electron and Proton Precipitations on Thermospheric Nitric Oxide Cooling During Shock-Led Interplanetary Coronal Mass Ejections

Cissi Y. Lin[1,2], Yue Deng[1], Delores J. Knipp[3,4], Liam M. Kilcommons[3], and Xiaohua Fang[5]

[1]Department of Physics, University of Texas at Arlington, Arlington, TX, USA, [2]Cooperative Institute for Research in Environmental Sciences, University of Colorado Boulder, Boulder, CO, USA, [3]Aerospace Engineering Sciences, University of Colorado Boulder, Boulder, CO, USA, [4]High Altitude Observatory, National Center for Atmospheric Research, Boulder, CO, USA, [5]Laboratory for Atmospheric and Space Physics, University of Colorado Boulder, Boulder, CO, USA

Key Points:

- Electrons play a dominant role, but protons also contribute around a quarter of the total NO cooling enhancement during geo-effective ICMEs
- Electrons of 1.4–30.2 keV are main contributors to NO cooling enhancement during geo-effective events
- Time lags for maximal correlation with electron precipitating energy flux are 1–6 hr longer for NO cooling than for TEC

Correspondence to:
Y. Deng,
yuedeng@uta.edu

Citation:
Lin, C. Y., Deng, Y., Knipp, D. J., Kilcommons, L. M., & Fang, X. (2019). Effects of energetic electron and proton precipitations on thermospheric nitric oxide cooling during shock-led interplanetary coronal mass ejections. *Journal of Geophysical Research: Space Physics*, *124*, 8125–8137. https://doi.org/10.1029/102019JA027089

Received 30 JUN 2019
Accepted 24 SEP 2019
Accepted article online 10 OCT 2019
Published online 30 OCT 2019

Abstract Satellite measurements have revealed significant enhancement of 5.3-μm nitric oxide (NO) emission during shock-led interplanetary coronal mass ejections. Great discrepancies in modeled neutral density occur during these events and may be attributed to the abnormally high NO cooling. Meanwhile, the relative significance of protons, soft electrons, and keV-electrons to NO emission is yet to be well determined. The goal of this study is to identify the contribution of electron and proton precipitations to the thermospheric NO cooling by using the Defense Meteorological Satellite Program (DMSP) data. The observed energetic electrons and protons (0.1–30.2 keV) during 36 shock-led interplanetary coronal mass ejection events in 2002–2010 are binned into geomagnetic grids to provide statistical distributions of the particle precipitation for polar regions. The distributions are incorporated into the Global Ionosphere-Thermosphere Model. The results show that electrons play a dominant role to NO cooling, but protons are also important and contribute to up to a quarter of NO cooling by electrons and ions combined. NO cooling enhancement during the events is proportional to the level of energy flux and is dominated by the electrons in the energy band of 1.4–3.1 keV. Both total electron content (TEC) and NO cooling enhance at the source regions, but they have different lifetime and correlation with the particle precipitations. Generally, NO cooling and TEC enhancements have a positive correlation with the precipitating energy. Cross correlation shows that particle precipitations have more instantaneous impact on TEC while it takes longer for the atmosphere to heat up for cooling to proceed.

1. Introduction

Energetic particles associated with geo-effective events, when precipitating into the upper atmosphere, initiate a chain of chemical reactions, cause intensive ionization leading to enhanced electron density (Fuller-Rowell et al., 1994), and result in additional heating leading to temperature increase (Roble & Ridley, 1987). Meanwhile, these sudden (and localized in most cases) changes can set off acoustic-gravity waves (Hocke & Schlegel, 1996; Hunsucker, 1982) in the forms of traveling atmospheric (Prölss & Jung, 1978) and ionospheric (Hajkowicz, 1990; Pradipta et al., 2016) disturbances. Simulations of precipitating soft particles into the dayside cusp region have shown that the precipitating electrons and protons lead to changes of 30% and −4% of the neutral density at 400 km, respectively (Deng et al., 2013).

Total electron content (TEC) is a widely used way for studying ionospheric response by utilizing the widespread global navigation satellite system receivers (Mendillo, 2006). As energetic particles and photons (or the lack of them) play a key role in the increase (or decrease) of the ionospheric electron density, the TEC variations have been found to associate with geomagnetic storms (e.g., Fuller-Rowell et al., 1994), solar flares (e.g., Liu et al., 2006), and solar eclipse (e.g., Lin, Deng, & Ridley, 2018; Zhang et al., 2017). Terrestrial events, such as tsunamis (Galvan et al., 2011; Saito et al., 2011; Tsugawa et al., 2011), earthquakes (e.g., Liu et al., 2001), volcanic eruptions (Dautermann et al., 2009; Shults et al., 2016), and weather systems (e.g., Nishioka et al., 2013) also induce upward-propagating waves which result in observable waves in TEC measurements. The TEC disturbances have also been observed to propagate across hemispheres (Zhang et al., 2003).

While the atmosphere heats, the cooling agents – nitric oxide (NO) via 5.3 μm and carbon dioxide via 15 μm —serve as thermostats (Mlynczak et al., 2003) to release the additional heat to maintain a well-balanced terrestrial atmosphere. It has been shown that precipitating electrons of 1–10 keV contribute to most of the NO production in the lower thermosphere (Barth et al., 2003). The energetic photons or particles of ~100 eV have the most efficient cross section for the NO production in the lower thermosphere (Yonker, 2013). The 1–10 keV photons and particles deposit most of their energy at the altitudinal range of 100–200 km (Fang et al., 2008; Fang et al., 2013; Solomon & Qian, 2005), where NO abundance is maximal, and are able to create multiple NO molecules efficiently for every depositing photon/particle through a chain of cascading reactions.

A superposed epoch analysis (SEA) has been used to study about 200 interplanetary coronal mass ejection (ICME) events with and without leading shocks and magnetic clouds (Knipp et al., 2017). The study shows that during shock-led events NO cooling evidently intensifies not only after ICME arrival but also up to two days prior, which may contribute to the abnormal features of neutral density variation during a storm period (Knipp et al., 2013). The feature of NO emission was found likely associated with the precipitating particles. Particularly, the energy flux of the electrons greater than 0.1 keV and that of the protons greater than 10 keV measured by the Defense Meteorological Satellite Program (DMSP) spacecraft show a similar temporal variation as NO emission.

While many previous studies have addressed NO cooling and its impact on the ionosphere and thermosphere, the primary mechanisms causing the discrepancies between modeled and observed NO emission enhancement and neutral density variation at the polar region have not been adequately quantified (Knipp et al., 2013). What roles do proton precipitation and electron precipitation play? Which energy band of electrons can impact observable NO cooling enhancement most effectively? In this study, a global circulation model for the upper atmosphere, Global Ionosphere-Thermosphere Model (GITM; Ridley et al., 2006), with the new photochemistry module (Lin, Deng, Venkataramani, et al., 2018; Lin & Deng, 2019) is used for investigating the impacts of the precipitating particles (electrons and protons) during shock-led events to address these concerns. Shock-led events, among the cases presented in Knipp et al. (2017), appear to associate with significant energy influx of both electrons and protons and to be best correlated with NO emission response to these precipitating particles. The possible causes for elevated particle precipitation during shock-led events are discussed in detail in Knipp et al. (2017). In section 2, a brief introduction to the GITM model is given and the implementation of the DMSP precipitation to GITM is explained in detail. In section 3, the consequential thermospheric and ionospheric responses to the precipitating particles are presented.

2. Methodology

2.1. Global Ionosphere-Thermosphere Model

Global Ionosphere-Thermosphere Model (GITM; Ridley et al., 2006) is a three-dimensional global circulation model for the upper atmosphere. Different from most of the conventional circulation models, GITM relaxes the hydrostatic assumption, has flexible grid resolutions, and short time steps of ~2 s. These features make, for example, realization of acoustic-gravity waves (Deng et al., 2008; Deng & Ridley, 2014; Lin et al., 2017; Lin, Deng, & Ridley, 2018), possible. A new photochemistry module was added to GITM for better accounting for the production of NO via meta-state of nitrogen and secondary electrons/photoelectrons to investigate the sensitivity of the global NO cooling power at various solar and geomagnetic activity levels (Lin, Deng, Venkataramani, et al., 2018). Utilizing the updated model, a climatological variation of global NO cooling shows a decadal decrease of −17% over the temporal span of 1982–2013 (Lin & Deng, 2019). The variation agrees well with that derived from the empirical thermospheric proxy by Mlynczak et al. (2016). In those studies, the GITM simulations were driven with the empirical precipitating patterns (Fuller-Rowell & Evans, 1987), for given solar wind conditions and hemispheric power, but without precipitating protons. Galand et al. (1999) suggested that precipitating protons played a larger role in ionospheric behavior than what has been previously appreciated. With the same photochemical configuration used in Lin, Deng, Venkataramani, et al. (2018) and Lin and Deng (2019), the simulations presented in this study are driven with the patterns deduced from binned DMSP measured electron and proton precipitation.

2.2. Satellite Measurements

Since 1960s, the U.S. Department of Defense initiated the spaceborne observations using low-earth-orbiting DMSP satellites. DMSP consists a suite of satellites that have been deployed over the years. With a regular

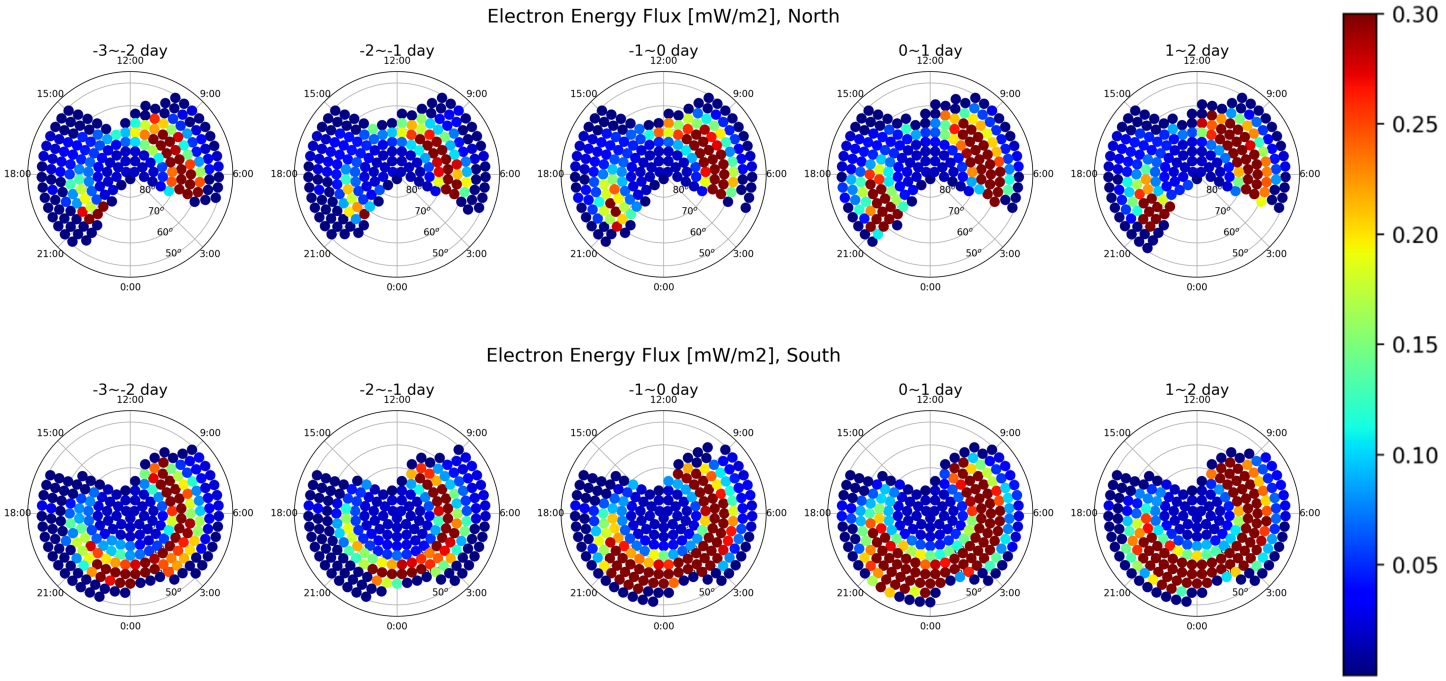

Figure 1. Statistically binned precipitation patterns of the Defense Meteorological Satellite Program (DMSP) Special Sensor J (SSJ) electron band (Band 3: 1.4–3.1 keV) during shock-led interplanetary coronal mass ejections (ICMEs) over the geomagnetic (top) north and (bottom) south poles. From left to right: superposed epoch analysis temporal intervals of day −3 to −2, −2 to −1, −1–0, 0–1, and 1–2.

launching schedule for sequential satellites, often more than one DMSP satellite is observing space environment at a given time. Its longevity in continuous data collection has made the DMSP data set one of the best data sets for climatological studies. The most recent series of DMSP, Block 5D-3, has a Sun-synchronous orbit altitude of ~850 km, an inclination of 98.8°, and an orbit period of 101 min. Currently, four DMSP satellites (F15, F16, F17, and F18) are still operational.

While the DMSP pass-integrated particle flux (as shown in Knipp et al. (2017)) is appropriate for the temporal comparison with other satellite measurements, pass-integrated flux cannot be directly implemented as the particle forcing for a global model since two-dimensional maps are needed to drive the global model. Thirty-six isolated shock-led ICME events in 2002–2010 are selected for this study with the criteria that no other obvious ICME disturbance has occurred in the 3 days prior (Knipp et al., 2017). To obtain continuous polar coverage of statistically meaningful precipitation maps for a five-day duration surrounding shock-led events, the DMSP particle flux measurements are binned into equal-area bins with a one-day cadence. In order to be implemented into GITM for the simulation purpose of this study, the 19 DMSP/Special Sensor J (SSJ) channels are categorized into four bands: (Band 1) 0.1–0.3 keV, (Band 2) 0.44–0.95 keV, (Band 3) 1.4–3.1 keV, and (Band 4) 4.4–30.2 keV. The energy bands were experimentally selected so that each band has sufficient numbers of measurements to provide a reasonably good precipitation pattern for the purpose of this study. See Kilcommons et al. (2017) and Redmon et al. (2017) for additional information about DMSP particle processing.

The resulting precipitating maps of Band 3 shown in Figure 1 provide a multi-day view of how the precipitating particle pattern varies with time in geomagnetic coordinates during the SEA intervals. We consider the interval three days ahead (−3) and two days subsequent (+2) to the shock onset at the epoch 0. Precipitating electrons are present throughout the 5-day interval, defining clear auroral ovals mostly poleward of 60°. The precipitating ovals start to expand to equatorward of 60° and the overall energy flux intensifies by ~50% slightly before epoch 0. Even with data gaps at the night side, the oval and the flux enhancement are also observable at the northern hemisphere. Similar to Figure 1, Figure 2 shows the evolution of the proton precipitation pattern in geomagnetic coordinates. The intensity of proton precipitation reaches its maximal level during day −1–0 and gradually returns to the preevent level for the following two days, unlike the electron

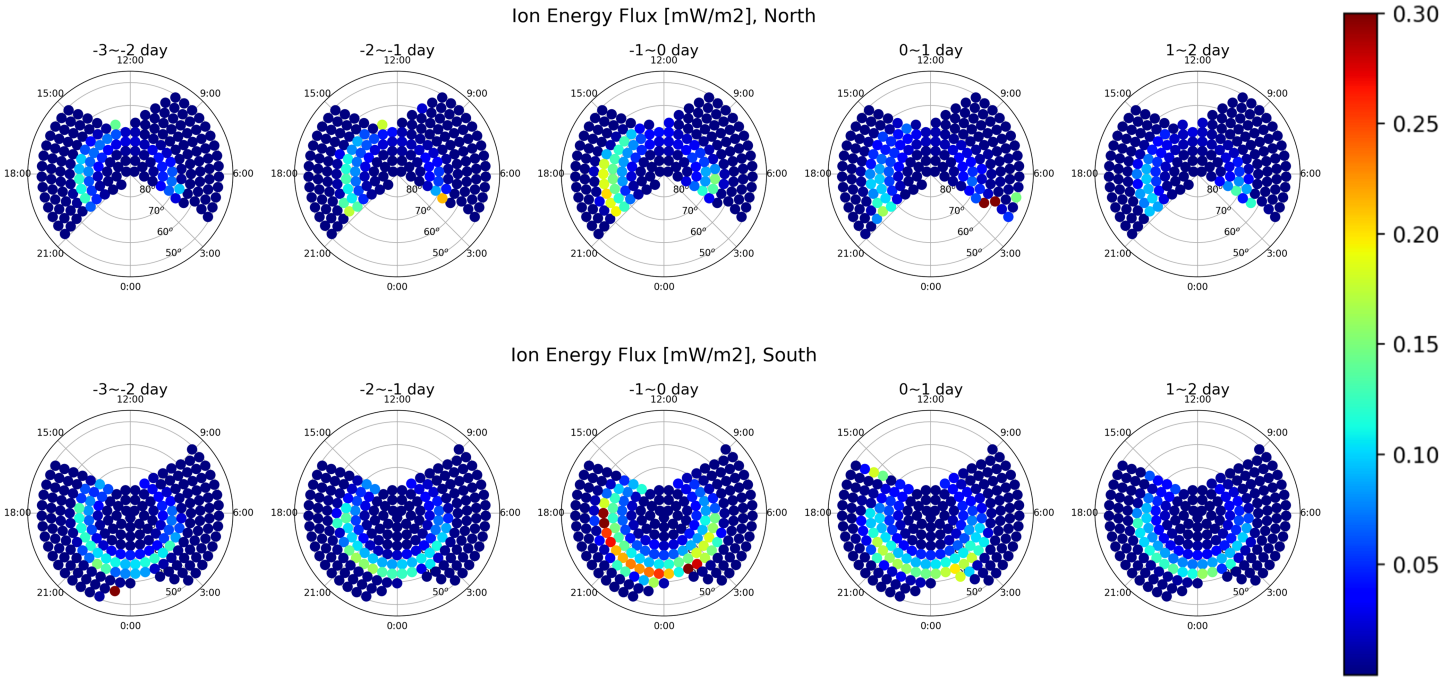

Figure 2. Similar to Figure 1 but for total Defense Meteorological Satellite Program (DMSP) Special Sensor J (SSJ) ion bands (0.1–30.4 keV).

precipitation, which remains elevated in the days after the shock. Because proton precipitation data can be sparser, all protons with energy of 0.1–30.2 keV are binned together for the statistical distributions.

Due to DMSP's Sun-synchronous orbits, particle precipitation observations are unavailable on the night side of the northern hemisphere, where the auroral forcing is critical, as well as on the day side of the southern hemisphere. To address the issue of data gaps, the following steps are taken to prepare the driving DMSP precipitation maps: (1) mapping into spherical geomagnetic grids, (2) merging the north and south precipitating patterns, and (3) applying a weighted smoothing window of 25 degrees zonally. From left to right, the first four panels of Figure 3 show examples of the precipitating particle maps for electrons of 0.1–0.3 keV, 0.44–0.95 keV, 1.4–3.1 keV, and 4.4–30.2 keV on the day of the event onset. Comparing the reprocessed Band 3 (middle panel of Figure 2) with the original map of 0–1 day in Figure 1 shows that the precipitating area slightly widens but the abrupt changes of energy flux at adjacent grids are smoothed. The total energy flux remains the same.

Similarly, the right panel of Figure 3 shows the reprocessed map for proton precipitation on the day of the event onset. In general, the energy level of proton flux is ~25% and ~10% of that of electron flux before

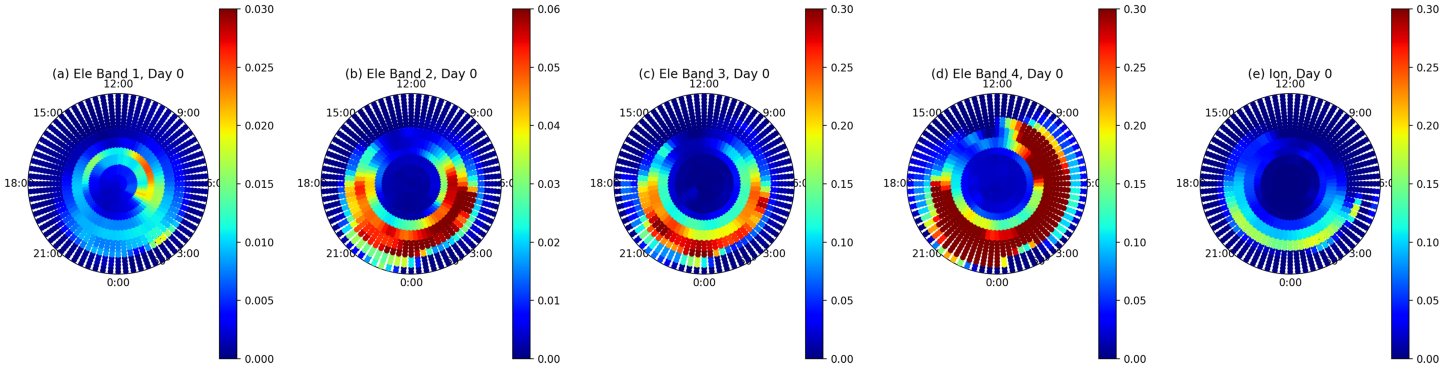

Figure 3. North-south merged and zonally smoothed precipitation patterns in the geomagnetic coordinates for the Defense Meteorological Satellite Program (DMSP) Special Sensor J (SSJ) electron and ion bands: (from left to right) 0.1–0.3, 0.44–0.95, 1.4–3.1, and 4.4–30.2 keV electrons and 0.1–30.2 keV ions on the day of the superposed epoch analysis event onset.

and after onset, respectively, for the cases studied. This level of proton precipitation has been neglected for decades (Fuller-Rowell & Evans, 1987) and may potentially cause discrepancies in estimating the thermospheric energy budget and consequential states of the upper atmosphere (Galand et al., 1999).

2.3. Ionization by Precipitating Particles

The DMSP precipitating electrons and protons characterized by their average energy (not shown) and energy flux (shown in Figures 1–3), show temporally and spatially varying patterns. To determine ionization rates, the spectrum of the precipitating particles is needed. Electrons are treated as Maxwellian as in diffuse aurora and as mono-energetic as in discrete aurora. Protons are treated as mono-energetic since proton precipitation is episodic. The parameterization for the mono-energetic particles has been developed and validated against first-principles models (Fang et al., 2010) and is used to characterize the precipitating electrons in each energy band and to determine the ionization profiles at each grid in this study (but we also used Maxwellian distributions to examine the total effect). As the altitude of maximal ionization varies with the energy of the influx, Maxwellian electrons and mono-energetic electrons, with the same average energy and total energy flux, are expected to have different impacts on the thermosphere and ionosphere. As the Maxwellian electron spectrum (Fuller-Rowell & Evans, 1987) prescribes electrons ranging from 0.3 to 20 keV, it is likely to result in a greater impact to a wider (thicker) altitudinal range compared to a band of mono-energetic electrons with the same total energy flux and average energy. For the precipitating protons, the parameterization of Fang et al. (2013) is used to determine the ionization profiles at each grid point.

For the sake of this study, the ionization rate mainly determines the production of NO. At a given simulation grid point, NO cooling is governed by NO and O density and the ambient temperature, which is the reason that the peak altitude of NO cooling differs from that of NO density. If the changes of the other two quantities are small enough and the system is at a steady state, presumably NO cooling is mainly governed by NO density, which depends highly on the ionization rate of molecular nitrogen. Further discussions regarding to NO density and cooling, particularly for the GITM photochemical scheme, can be found in Lin, Deng, Venkataramani, et al. (2018).

2.4. Simulation Setup

To ramp up the simulation, a 3-day preconditioning of the model has been performed without any particle precipitation. Since the statistical availability of the DMSP observations comes from various solar activity levels (Figure 2 of Knipp et al., 2017), a modest value (150 sfu) of the F10.7 index is used throughout the simulation period and the time frame is set around the equinox for the sake of simplicity. The simulation duration for each precipitating scenario is ten days. The DMSP particle forcing is switched on for the first five-day interval and switched off afterwards—a *precipitating case*. In the 5-day window, the DMSP precipitating particle pattern (in geomagnetic coordinates) updates once a day, and its impact on the terrestrial atmosphere updates at every GITM simulation time step (~2 s) in geographic coordinates. A zero-precipitation run is performed as a *base case*. The interplanetary magnetic field and solar wind condition are kept modestly the same for the precipitating case and the base case so that the difference between the two can be interpreted as the impact on the ionosphere and thermosphere (IT) contributed solely by the precipitating forcing.

3. Results

In this section, we first show the overall impacts of the precipitating electrons and protons to the IT system in terms of variations in electron number density, neutral mass density, and temperature. Consequentially, these variations lead to the enhancement of TEC and NO cooling. Then, we investigate the contribution of each electron band and the integrated proton band separately. Lastly, thermospheric and ionospheric responses at the polar region during the precipitating events are discussed.

3.1. Precipitating Energy and NO Cooling

During the precipitating events, additional energy influx increases ionization as well as heats the upper atmosphere. A chain of photochemical reactions is initiated and the atmosphere is set to re-balance the impact caused by the additional energy. These sudden and localized variations also launch acoustic-gravity waves (Deng et al., 2008). Figure 4 shows the northern polar views of the electron (top panels) and proton (bottom panels) precipitating patterns and their consequences to the IT system in the geographical coordinates. The seemingly discontinuous precipitation patterns in Figures 4a and 4b are owing to the combined effects

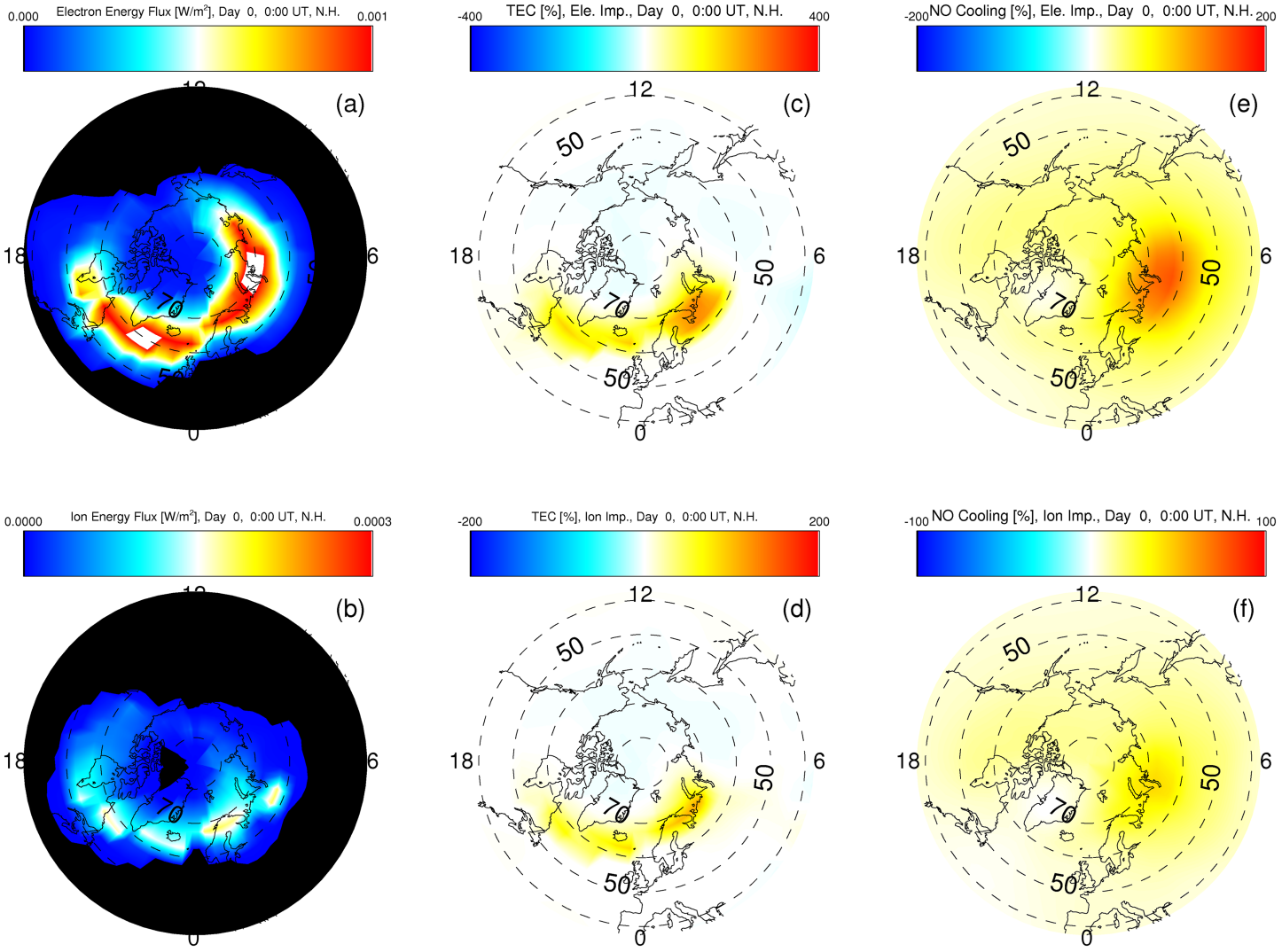

Figure 4. (a and b) Northern polar view of the (top row) total electron and (bottom row) ion precipitation and their impact to the (c and d) total electron content and (e and f) NO cooling.

from the grid resolution and the geomagnetic-geographic coordinate transform process. The precipitating electrons and protons result in additional ionization at the altitudes of 100–250 km and 100–200 km, respectively (Fang et al., 2010, 2013). They lead to increases of the electron density as shown in the TEC maps in Figures 4c and 4d. The maximal TEC increases of factors of 4 and 2 for the electron and proton precipitation, respectively. The spatial distribution of TEC enhancement appear to correlate well with that of instantaneous precipitation pattern because the ionospheric electrons are created almost instantaneously when the energy deposits. Meanwhile, more NO molecules are created through the photochemical processes. Being a good thermostat of the upper atmosphere (Mlynczak et al., 2003), NO is the dominant agent releasing the additional energy back to the space via infrared at 5.3 μm. For the shock-led events, Figure 3 shows that there is a higher concentration of precipitating energy at the pre-dawn and dawn side, especially Bands 3–4. Consequentially, as NO abundance increases during the precipitating events, the enhancement of the altitudinally integrated NO cooling can be observed as well as in Figures 4e and 4f. The precipitating particles of a few keV at the predawnside and dawnside likely associate with intense field-aligned currents as a result of magnetic and velocity shears in the magnetosphere during shock aurora (Zhou et al., 2017). Overall, the NO cooling enhancement occurs with the particle precipitation. It is worth noting that NO cooling enhances in a more expansive and extensive manner while the particles precipitate mostly poleward of 50°. Similar features have been previously observed (e.g.,

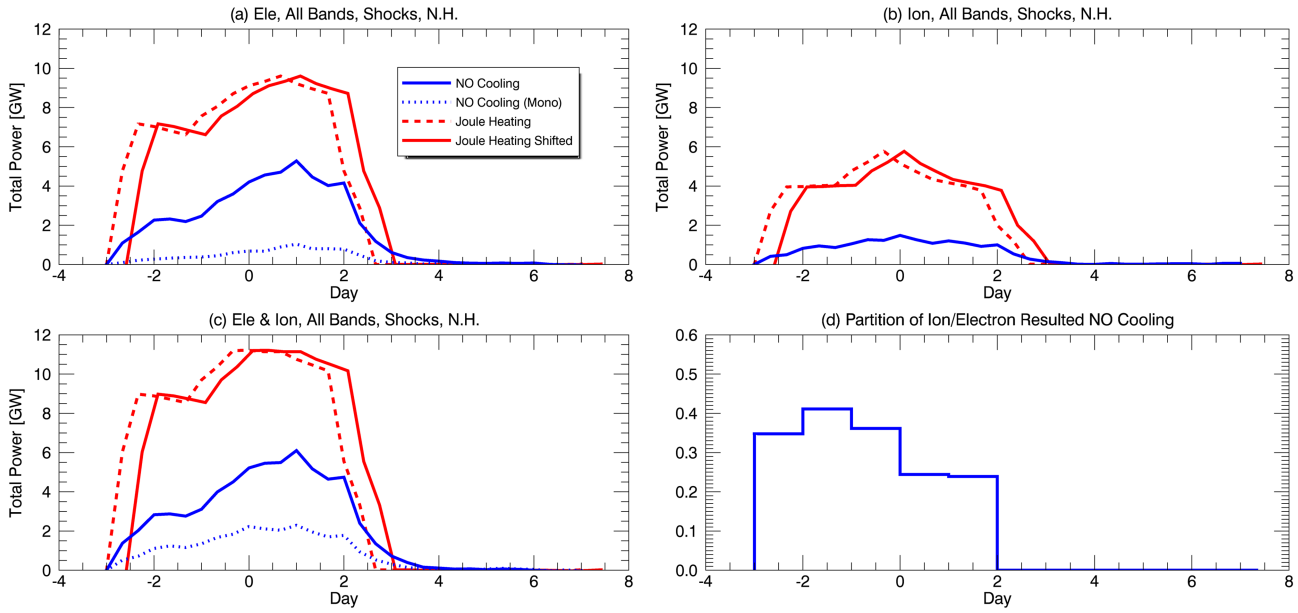

Figure 5. Enhancement of total NO cooling power (blue) poleward of 40°N with (a) electron-only, (b) ion-only precipitation, and (c) both electron and ion. Electrons are characterized as Maxwellian (solid blue) as well as mono-energetic (dotted blue). A time lag of 8 hr (solid red) is applied to the 24-hr smoothed total Joule heating for the cases with the Maxwellian electrons. The time lag improves the correlation coefficient from 92% (between solid blue and solid red) to 96% (between solid blue and dashed red). (d) The ratio of the contributed NO cooling enhancement by ions over that by electrons are further derived from daily averages with respect to the superposed epoch analysis epochs to facilitate future accounting of the ion contribution.

Flynn et al., 2018). The cooling rate via the 5.3-μm channel depends not only on the NO density but is also modulated by O density and temperature (Kockarts, 1980). With the mixture of NO density and temperature increases and the highly varying O distribution, the altitudinally integrated NO cooling enhancement provides an overall representation of the complexity of the thermospheric energy re-balancing during the events.

While Figure 4 shows the spatial distribution of the modeled IT responses to the incoming energy at a point in time, Figure 5 provides the temporal evolution. The enhancement of integrated NO cooling (in blue) northward of 40°N with precipitation from the simulations with (a) both electrons and protons, (b) electrons alone, and (c) protons alone. The zero-epoch corresponds to ICME arrival – the arrival of the ejecta leading edge at the upstream spacecraft (Chi et al., 2016). First, in Figure 5a, the enhancement of NO cooling peaks (~5 GW) toward the end of Day 1 when the intensity of the precipitating electrons reaches its maximal level (a total energy of ~19 GW) during Day 0–1 (as shown in Figure 1). As the reactions to create NO through energetic particles are fast, NO abundance builds up almost instantaneously with the precipitating electrons. Additionally, NO molecules have a lifetime of ~1 day (Solomon et al., 1999), during which these additionally created NO molecules stay in the thermosphere to continue cooling the atmosphere. After the precipitating forcing is turned off at the end of Day 2, NO cooling starts to decrease but remains positive through the rest of the simulation. Figure 5b depicts a similar story but for the proton precipitation. Instead, NO cooling peaks at Day 0 since the proton precipitation is strongest during Day −1–0 (as shown in Figure 2). For the case in which both electrons and protons are precipitating, the resulting enhancement of NO cooling shown in Figure 5c is about the same magnitude as the two in Figures 5a and 5b combined. Since the north and south hemispheres are driven by the same re-processed DMSP patterns as discussed in section 2, the results of the south hemisphere conclude similarly and therefore not shown here. By taking the ratio of the daily averaged NO cooling enhancement by protons and that by electrons, the relative partitions with respect to the SEA epochs as shown in Figure 5d may serve as simple multipliers for the models that only implement electron precipitation to account for prospective proton precipitation. Overall, proton precipitation is shown to result in NO cooling enhancement as much as 30% of that resulting from electron precipitation and accounts for a quarter of the total cooling enhancement. Therefore, its impact to the energy budget of the thermosphere should not be ignored and deserves careful investigations.

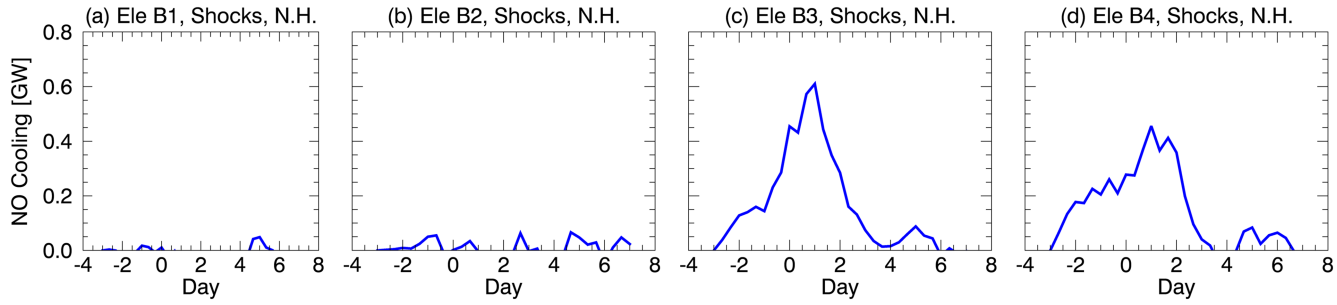

Figure 6. Enhancement of total NO cooling power poleward of 40°N by (a) Band 1, (b) Band 2, (c) Band 3, and (d) Band 4 electrons. Overall, Bands 3–4 contribute to 53% and 47%, respectively, of the total NO cooling enhancement when all four bands are implemented together (dashed line in Figure 5(b)) whereas the contributions of Bands 1–2 are negligible.

Galand et al. (1999) demonstrated that including Maxwellian-distributed protons of 1–20 keV into the Thermosphere-Ionosphere Electrodynamic General Circulation Model (TIE-GCM) not only leads to more proton production but also results in NO density increases of as high as 53% at the altitudinal range of 100–160 km. Though the precipitating protons are characterized differently—mono-energetic in this work versus Maxwellian-distributed in Galand et al. (1999), the magnitude of the increases of NO density and cooling owing to the inclusion of the proton precipitation agree well to the first order.

On the other hand, enhancement of NO cooling is the result of the additional thermospheric heating. Mlynczak et al. (2005) shows that SABER NO emission at 5.3 μm accounts for 28% of the combined energy of Joule heating and auroral dissipation provided by the Assimilative Mapping of Ionospheric Electrodynamics (AMIE) procedure (Richmond & Kamide, 1988) during the April 2002 storm. The TIE-GCM simulations with AMIE forcing show that global NO cooling power accounts for ~80% of Joule heating energy input and correlates well with 20- to 24-hr averaged Joule heating with a time lag of 8–10 hr (Lu et al., 2010). The dashed red lines in Figure 5 show the 24-hr averaged Joule heating and the solid red lines show that with an 8-hr delay. The 8-hr temporal delay improves the correlation coefficient between the integrated NO cooling and Joule heating from 92 to 96%. Over the 10-day simulations under the three scenarios presented in Figure 5, the total Joule heating is roughly 2–3 times greater than the total particle energy and roughly equal to the total amount of NO cooling (not shown). The total *enhanced* Joule heating (the difference between the precipitating cases and the base case) is about 70% of the enhanced energy of the precipitating particles as a result of the increase of conductance. The total reduced energy through the enhanced NO cooling is about 30–50% of that of the Joule heating.

Furthermore, we investigate the contribution of each electron band by implementing the electron bands separately. Again, Bands 1–4 contain electrons of 0.1–0.3, 0.44–0.95, 1.4–3.1, and 4.4–30.2 keV, respectively. Figure 6 from left to right shows their contributions to the resulting NO cooling enhancement. Clearly Band 3 and Band 4 contain most of the energy and dominate the associated NO cooling response. Of the two, Band 3 also has higher value of energy flux (even though with a lower average energy) and results in greater NO cooling enhancement. Overall, Bands 3 and 4 result in 53%, and 47%, respectively, of total NO cooling enhancement when the four bands are implemented altogether whereas the contributions of Bands 1 and 2 are negligible.

The fact that the enhancement of NO cooling during the events from our simulations presents an almost linear relation to the precipitating forcing is not surprising. In general, the altitude, at which the incoming flux (whether energetic particles or photons) mostly deposits, is determined by its energy band and the atmospheric cross sections (Solomon & Qian, 2005). Particularly, for the mono-energetic electrons and protons that are assumed for the simulations in this study, it is shown that the ionization peak altitudes are at 230 km and 105 km for 0.1 keV and 10 keV electrons, respectively, (Fang et al., 2010) and 170 km for 0.1 keV and 120 km for 10 keV protons, respectively, (Fang et al., 2013). Since the most impacted altitudes by the electrons and protons at different energy bands are distinct, collectively the consequential IT responses are linear to the first order.

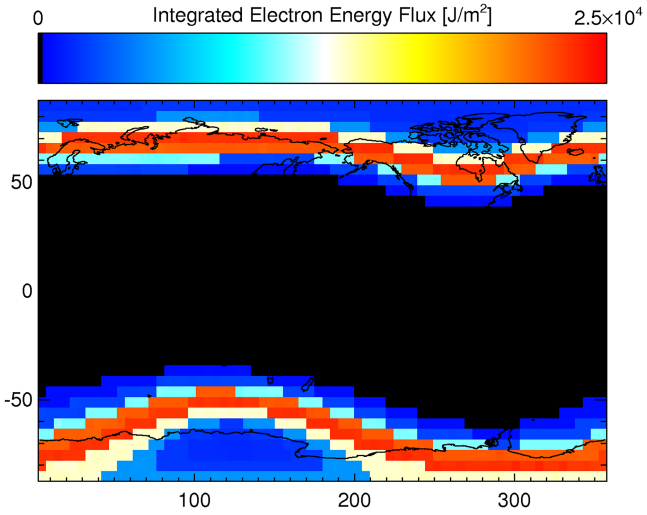

Figure 7. Five-day integration of the precipitating energy by electrons.

3.2. Correlations With the Precipitation Patterns

From Figures 4–6, a clear link is observable between the particle forcing and the enhancement of NO cooling and TEC as discussed in the previous sections. To investigate the link more closely, we use the electron case as an example and construct time series of the SSJ energy flux, NO cooling, and TEC enhancement to evaluate the correlation coefficients between the forcing and responses at each grid point. To facilitate further interpretation of the results, Figure 7 shows the maps of five-day integration of the precipitating energy by electrons. All subsequent figures show the discrete levels of the color bar better and thus have the mosaic appearance to emphasize the values at grid points. The global correlation coefficient maps in Figure 8 show the longitudinal and latitudinal variations of (a) TEC and (b) NO cooling correlated with the SSJ electron precipitation pattern. Corresponding to the black band in Figure 7, the white area equatorward of ~40° indicates that no SSJ precipitation data (equatorward of geomagnetic latitude 50°) is available. A strong correlation between the particle forcing and both the TEC and NO cooling enhancement is clearly observable at the precipitating ovals. Patches with low and negative correlation are particularly noticeable in the TEC correlation coefficient map in Figure 8a. Outside of the ovals, correlations are low for TEC but remain high for NO cooling. Particle precipitations during geo-effective events often initiate traveling ionospheric disturbances (TIDs). These TIDs have been observed in TEC observations (e.g., Hajkowicz, 1990; Pradipta et al., 2016) as well as GCM simulations, including GITM (Guo et al., 2018; Lin, Deng, Venkataramani, et al., 2018). These TIDs can travel away from the source region, such as the auroral zone. The low and negative correlations in Figure 8a are likely caused by the dynamic of TEC variations, where the outward propagating TEC enhancement collocates with low precipitation area. Direct interpretation from the correlation coefficient maps of NO cooling (Figure 8b) is slightly trickier as NO cooling depends on not only NO density but also O density and the ambient temperature. As precipitation intensifies, the production and re-distribution of these species occurs and the ambience temperature changes. NO cooling enhancement represents a mixture of re-distributions of these "ingredients." Nevertheless, the general tendency of NO cooling associated with the precipitating energy is positive.

Time lags are then applied to the time series of the TEC and NO cooling enhancement to investigate the IT response time. Figure 9 shows the global distribution of time lags required for the TEC and NO cooling to

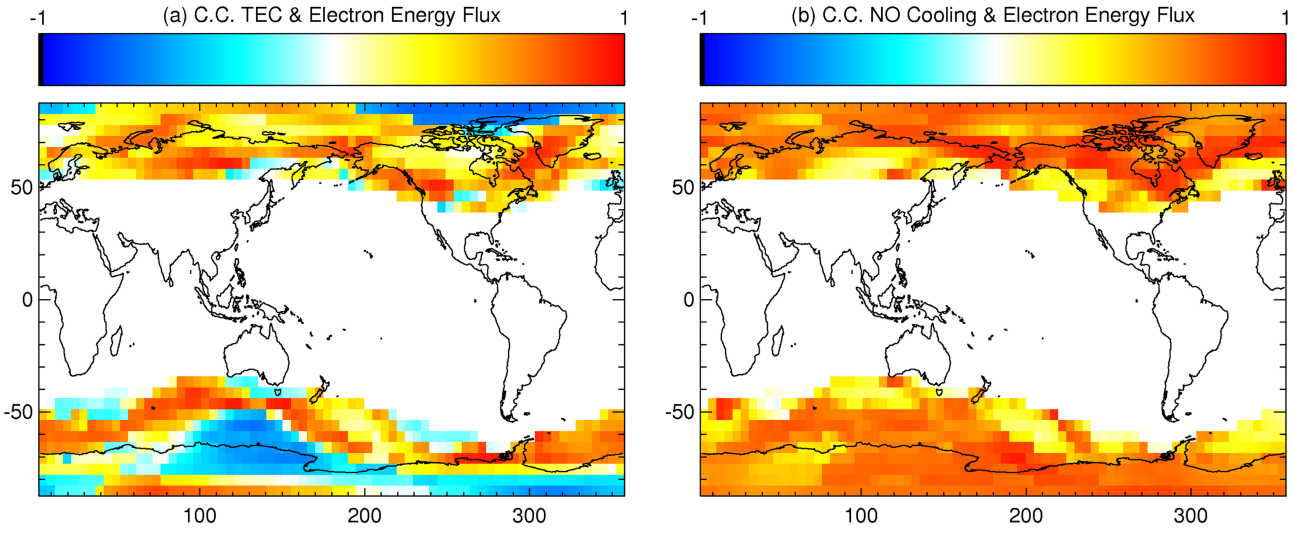

Figure 8. Correlation coefficient maps of (a) total electron content and (b) NO cooling with the Special Sensor J (SSJ) electron precipitations. The white area equatorward of ~40° indicates that no SSJ precipitation data (equatorward of geomagnetic latitude 50°) is available.

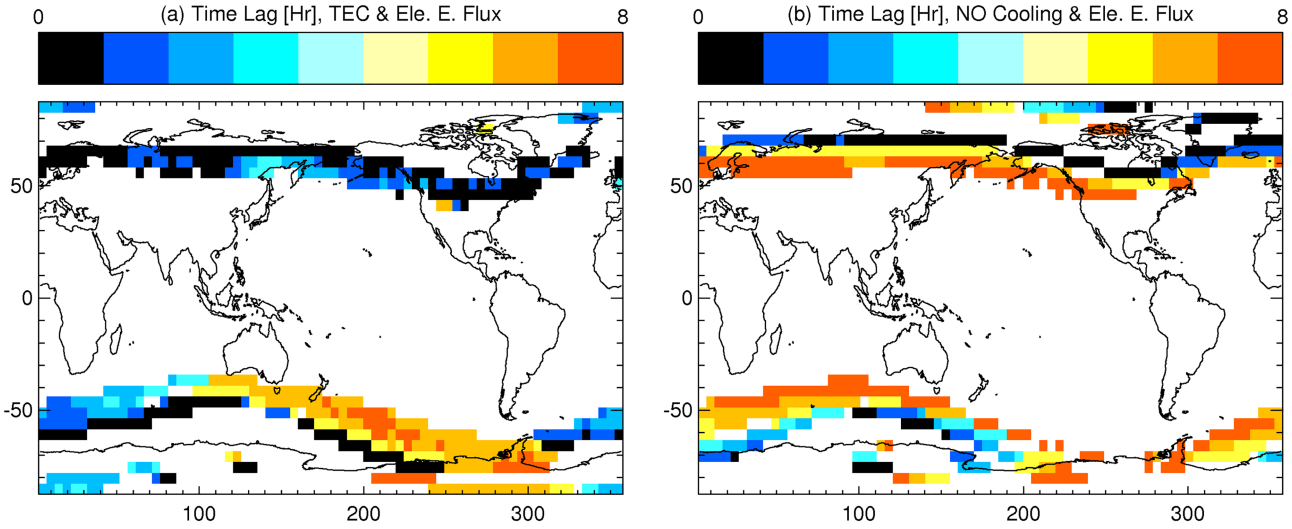

Figure 9. Time lags in hours required to obtain maximal correlation (shown in Figure 10) between precipitating electrons and (left) total electron content (TEC)/(right)NO cooling enhancement.

reach local maximal correlation (shown in Figure 10) with the precipitation energy by electrons. For the current demonstration, time lags longer than 8 hr are out of our interest and therefore treated as non-correlating (shaded in white). Our intent is to distinguish the differences of the shorter time lags between the TEC and NO cooling responses. The temporal resolution of this comparison is, however, limited by the output cadence to 1 hr. Readers' attention may be drawn to the narrow black strips poleward of the color contour in both panels. These black strips indicate time lags of shorter than 1 hr for maximal correlation. Comparing with the precipitating energy in Figure 8 shows that the time lags of 0–1 hr corresponding mostly to the strongest precipitating energy in the middle of the electron precipitation ovals. With these time lags, the maximal correlation coefficients at the locations with strong precipitation are in general greater than 0.7 as shown in Figure 10. On the other hand, the estimated time lags increase moving toward the edges of the precipitation pattern where the precipitating energy is low.

A combination of several factors results in such a distribution. The search for maximal correlation shows that correlation decreases at a faster rate versus the time lag at locations with strong precipitation but at a slower

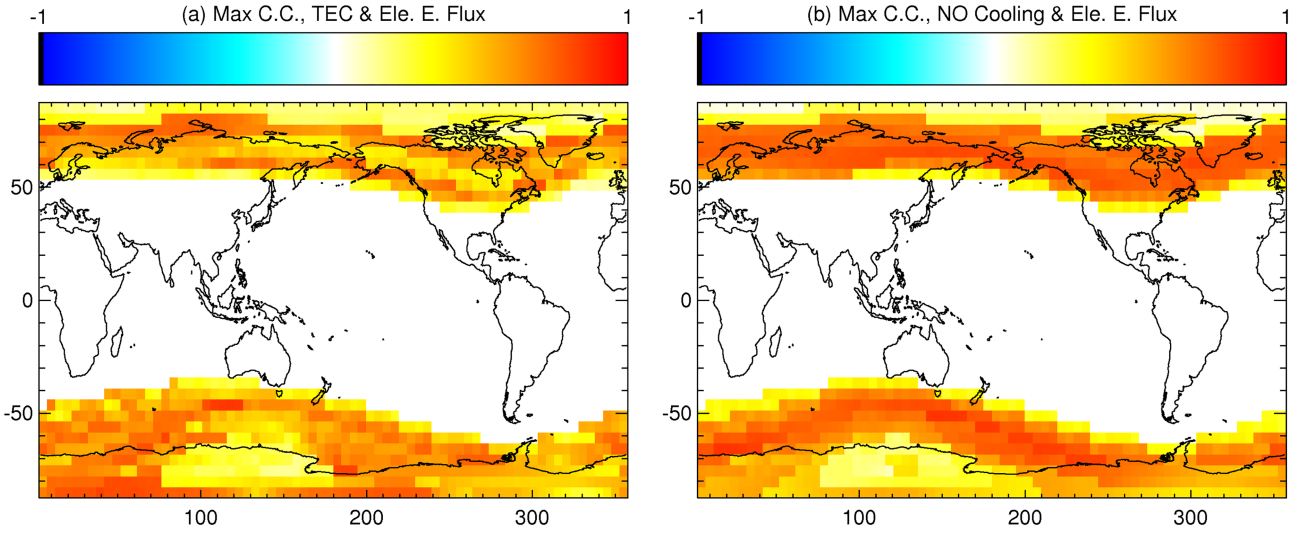

Figure 10. Maximal correlation coefficients between precipitating electrons and (left) total electron content (TEC)/(right) NO cooling enhancement reached at time lags shown in Figure 9.

rate where precipitation is weak. This results in a more defined time lag curve for area with strong precipitation and slightly ambiguous curve for areas with weak precipitation. We also note that the numerical process of obtaining the maximal correlation might have played a part. However, the combination of weaker ionization and higher-altitude ionization peak, and outward propagating enhancement from the band of strong precipitation may also contribute to strong correlations at the obtained time lags. Moreover, away from black strip of 0-hr lag in the southern hemisphere, there are two distinct groups: one with time lags of 1–4 hr and the other with time lags of 5–8 hr. The location of the latter group corresponds to the locations (between the geographical longitudes of 100–300°E, which is ~180° away from the geomagnetic south pole in longitude) where the longitudinal variation of the geomagnetic latitude of aurora oval during one day in the southern hemisphere is greater than that in the northern hemisphere, which corresponds to a more deviated (or "wobbling") precipitation pattern throughout the simulation period. Such a feature, however, is less significant for the northern hemisphere. Longitudinal dependency of the ionospheric and thermospheric constituents has long been observed (e.g., Cravens & Stewart, 1978; Kaufmann et al., 1976). Using Time Dependent Ionospheric Model, Sojka et al. (2012) found that electric field and thermospheric wind contribute to 10–20% of TEC variation, which results in longitudinal-dependency of the storm-time response. These proposed mechanisms may explain partially the longitudinal variation of time lags in Figure 9. Further examination needs to be conducted to better understand the model response time regarding NO cooling and TEC. Further conducting comparisons of response time between model results and observations will improve space weather prediction.

Comparing the left panels and the right ones in Figure 9 reveals another interesting perspective. For most part of the area of interest, the time lags are longer for the NO cooling enhancement than for the TEC enhancement. On average, time lags for NO cooling are 1–6 hr longer than those for TEC. This indicates that the TEC enhancement responds more directly and instantaneously to the precipitating particles than the NO cooling enhancement. Ionization, resulting in increases of electron density, occurs rapidly when the energy deposits. As NO cooling enhancement comes from additional NO production and increases of the ambient temperature as a result of energy deposition during geo-effective events, slight delays are reasonable and in agreement with Lu et al. (2010).

4. Summary

While it is well known that particle precipitation is the primary mechanism for the NO emission enhancement at the polar region, the relative significance of protons, soft electrons, and keV electrons is yet to be determined in a self-consistent manner. In this study, energetic particles measured by the DMSP satellites during shock-led ICME events have been implemented into the GITM model. The results reveal that electrons accounts for most of the NO cooling, but low-energy protons also contribute significantly and should be considered in the thermospheric energy budget estimation during geo-effective events.

By separately implementing particle energy bands, we show that the NO cooling enhancement responds almost linearly to the particle bands owing to the distinct energy-dependent ionization peaks among these energy bands. Among four electron bands, NO cooling enhancement during the particle precipitating events is proportional to the level of energy flux and is dominated by the energy flux of the electrons in the energy band of 1.4–3.1 keV (ionization peak at 100–200 km). By constructing time series of the TEC and NO cooling enhancement and correlating them with the precipitating energy at each simulation grid, we show how the global ionosphere (TEC) and thermosphere (NO cooling) response temporally and spatially. The global thermospheric and ionospheric responses show that both TEC and NO cooling enhance instantaneously at the source regions, but they have different lifetimes and correlations with the particle precipitations. In general, the NO cooling and TEC enhancement with the precipitating energy has positive correlation. Cross correlation shows that time lags for maximal correlation for NO cooling tend to be 1–6 hr longer that those for TEC. Our results show that particle precipitations have more direct and instantaneous impact on TEC enhancement while it takes a little longer for the atmosphere to be heated for the cooling to proceed. The variation of geomagnetic coordinates and outward propagation of the enhancement may have caused the distinct feature of the obtained time lags equatorward of the strongest precipitation band in the southern hemisphere. Further investigation into the causal links among ICMEs, interplanetary magnetic field, and the magnetospheric processes is necessary.

Acknowledgments

This research at the University of Texas at Arlington was supported by NSF through grant ATM0955629, NASA through grants NNX13AD64G and NNX14AD46G, and AFOSR through awards FA9550-16-1-0059 and MURI FA9559-16-1-0364. The authors acknowledge the Texas Advanced Computing Center (TACC) at the University of Texas at Austin for providing Lonestar5 and Maverick resources that have contributed to the research results reported within this paper. URL: http://www.tacc.utexas.edu. The GITM model outputs are available at https://doi.org/10.5281/zenodo.3455854.

References

Barth, C. A., Mankoff, K. D., Bailey, S. M., & Solomon, S. C. (2003). Global observations of nitric oxide in the thermosphere. *Journal of Geophysical Research*, *108*(A1), 1027. https://doi.org/10.1029/2002JA009458

Chi, Y., Shen, C., Wang, Y., Xu, M., Ye, P., & Wang, S. (2016). Statistical Study of the Interplanetary Coronal Mass Ejections from 1995 to 2015. *Solar Physics*, *291*(8), 2419–2439. https://doi.org/10.1007/s11207-016-0971-5

Cravens, T. E., & Stewart, A. I. (1978). Global morphology of nitric oxide in the lower E region. *Journal of Geophysical Research*, *83*(A6), 2446–2452. https://doi.org/10.1029/JA083iA06p02446

Dautermann, T., Calais, E., & Mattioli, G. S. (2009). Global Positioning System detection and energy estimation of the ionospheric wave caused by the 13 July 2003 explosion of the Soufrière Hills Volcano, Montserrat. *Journal of Geophysical Research*, *114*, B02202. https://doi.org/10.1029/2008JB005722

Deng, Y., Fuller-Rowell, T. J., Ridley, A. J., Knipp, D., & Lopez, R. E. (2013). Theoretical study: Influence of different energy sources on the cusp neutral density enhancement. *Journal of Geophysical Research: Space Physics*, *118*, 2340–2349. https://doi.org/10.1002/jgra.50197

Deng, Y., Richmond, A. D., Ridley, A. J., & Liu, H.-L. (2008). Assessment of the non-hydrostatic effect on the upper atmosphere using a general circulation model (GCM). *Geophysical Research Letters*, *35*, L01104. https://doi.org/10.1029/2007GL032182

Deng, Y., & Ridley, A. J. (2014). Simulation of non-hydrostatic gravity wave propagation in the upper atmosphere. *Annales de Geophysique*, *32*, 443–447. https://doi.org/10.5194/angeo-32-443-2014

Fang, X., Lummerzheim, D., & Jackman, C. H. (2013). Proton impact ionization and a fast calculation method. *Journal of Geophysical Research: Space Physics*, *118*, 5369–5378. https://doi.org/10.1002/jgra.50484

Fang, X., Randall, C. E., Lummerzheim, D., Solomon, S. C., Mills, M. J., Marsh, D. R., et al. (2008). Electron impact ionization: A new parameterization for 100 eV to 1 MeV electrons. *Journal of Geophysical Research*, *113*, A09311. https://doi.org/10.1029/2008JA013384

Fang, X., Randall, C. E., Lummerzheim, D., Wang, W., Lu, G., Solomon, S. C., & Frahm, R. A. (2010). Parameterization of monoenergetic electron impact ionization. *Geophysical Research Letters*, *37*, L22106. https://doi.org/10.1029/2010GL045406

Flynn, S., Knipp, D. J., Matsuo, T., Mlynczak, M., & Hunt, L. (2018). Understanding the global variability in Thermospheric nitric oxide flux using empirical orthogonal functions (EOFs). *Journal of Geophysical Research: Space Physics*, *123*, 4150–4170. https://doi.org/10.1029/2018JA025353

Fuller-Rowell, T. J., Codrescu, M. V., Moffett, R. J., & Quegan, S. (1994). Response of the thermosphere and ionosphere to geomagnetic storms. *Journal of Geophysical Research*, *99*(A3), 3893–3914. https://doi.org/10.1029/93JA02015

Fuller-Rowell, T. J., & Evans, D. S. (1987). Height-integrated Pedersen and Hall conductivity patterns inferred from the TIROS-NOAA satellite data. *Journal of Geophysical Research*, *92*(A7), 7606–7618. https://doi.org/10.1029/JA092iA07p07606

Galand, M., Roble, R. G., & Lummerzheim, D. (1999). Ionization by energetic protons in Thermosphere-Ionosphere Electrodynamics General Circulation Model. *Journal of Geophysical Research*, *104*(A12), 27,973–27,989. https://doi.org/10.1029/1999JA900374

Galvan, D. A., Komjathy, A., Hickey, M. P., & Mannucci, A. J. (2011). The 2009 Samoa and 2010 Chile tsunamis as observed in the ionosphere using GPS total electron content. *Journal of Geophysical Research*, *116*, A06318. https://doi.org/10.1029/2010JA016204

Guo, J.-P., Deng, Y., Zhang, D.-H., Lu, Y., Sheng, C., & Zhang, S.-R. (2018). The effect of subauroral polarization streams on ionosphere and thermosphere during the 2015 St. Patrick's Day storm: Global ionosphere-thermosphere model simulations. *Journal of Geophysical Research: Space Physics*, *123*, 2241–2256. https://doi.org/10.1002/2017JA024781

Hajkowicz, L. A. (1990). A global study of large scale travelling ionospheric disturbances (TIDS) Following a step-like onset of auroral substorms in both hemispheres. *Planetary and Space Science*, *38*(7), 913–923. https://doi.org/10.1016/0032-0633(90)90058-X

Hocke, K., & Schlegel, K. (1996). A review of atmospheric gravity waves and travelling ionospheric disturbances: 1982–1995. *Annales Geophysicae*, *14*, 917–940. https://doi.org/10.1007/s00585-996-0917-6

Hunsucker, R. D. (1982). Atmospheric gravity waves generated in the high-latitude ionosphere: A review. *Reviews of Geophysics*, *20*(2), 293–315. https://doi.org/10.1029/RG020i002p00293

Kaufmann, P., Piazza, L. R., Massambani, O., Diniz Borges, V. N., & Koppe, E. H. (1976). Longitudinal dependence of ionospheric total electron content in the South Atlantic Geomagnetic Anomaly. *Nature*, *261*, 677–679.

Kilcommons, L. M., Redmon, R. J., & Knipp, D. J. (2017). A new DMSP magnetometer and auroral boundary data set and estimates of field-aligned currents in dynamic auroral boundary coordinates. *Journal of Geophysical Research: Space Physics*, *122*, 9068–9079. https://doi.org/10.1002/2016JA023342

Knipp, D., Kilcommons, L., Hunt, L., Mlynczak, M., Pilipenko, V., Bowman, B., et al. (2013). Thermospheric damping response to sheath-enhanced geospace storms. *Geophysical Research Letters*, *40*, 1263–1267. https://doi.org/10.1002/grl.50197

Knipp, D. J., Pette, D. V., Kilcommons, L. M., Isaacs, T. L., Cruz, A. A., Mlynczak, M. G., et al. (2017). Thermospheric nitric oxide response to shock-led storms. *Space Weather*, *15*, 325–342. https://doi.org/10.1002/2016SW001567

Kockarts, G. (1980). Nitric oxide cooling in the terrestrial thermosphere. *Geophysical Research Letters*, *7*, 137–140. https://doi.org/10.1029/GL007i002p00137

Lin, C. Y., & Deng, Y. (2019). Nitric oxide in climatological global energy budget during 1982–2013. *Journal of Geophysical Research: Space Physics*, *124*, 782–789. https://doi.org/10.1029/2018JA025902

Lin, C. Y., Deng, Y., & Ridley, A. (2018). Atmospheric gravity waves in the ionosphere and thermosphere during the 2017 solar eclipse. *Geophysical Research Letters*, *45*, 5246–5252. https://doi.org/10.1029/2018GL077388

Lin, C. Y., Deng, Y., Sheng, C., & Drob, D. P. (2017). A study of the nonlinear response of the upper atmosphere to episodic and stochastic acoustic-gravity wave forcing. *Journal of Geophysical Research: Space Physics*, *122*, 1178–1198. https://doi.org/10.1002/2016JA022930

Lin, C. Y., Deng, Y., Venkataramani, K., Yonker, J., & Bailey, S. M. (2018). Comparison of the thermospheric nitric oxide emission observations and the Global Ionosphere-Thermosphere Model (GITM) simulations: Sensitivity to solar and geomagnetic activities. *Journal of Geophysical Research: Space Physics*, *123*, 10,239–10,253. https://doi.org/10.1029/2018JA025310

Liu, J. Y., Chen, Y. I., Chuo, Y. J., & Tsai, H. F. (2001). Variations of ionospheric total electron content during the Chi-Chi Earthquake. *Geophysical Research Letters*, *28*, 1383–1386. https://doi.org/10.1029/2000GL012511

Liu, J. Y., Lin, C. H., Chen, Y. I., Lin, Y. C., Fang, T. W., Chen, C. H., et al. (2006). Solar flare signatures of the ionospheric GPS total electron content. *Journal of Geophysical Research*, *111*, A05308. https://doi.org/10.1029/2005JA011306

Lu, G., Mlynczak, M. G., Hunt, L. A., Woods, T. N., & Roble, R. G. (2010). On the relationship of Joule heating and nitric oxide radiative cooling in the thermosphere. *Journal of Geophysical Research*, *115*, A05306. https://doi.org/10.1029/2009JA014662

Mendillo, M. (2006). Storms in the ionosphere: Patterns and processes for total electron content. *Reviews of Geophysics*, *44*, RG4001. https://doi.org/10.1029/2005RG000193

Mlynczak, M., Martin-Torres, F. J., Russell, J., Beaumont, K., Jacobson, S., Kozyra, J., et al. (2003). The natural thermostat of nitric oxide emission at 5.3 μm in the thermosphere observed during the solar storms of April 2002. *Geophysical Research Letters*, *30*(21), 2100. https://doi.org/10.1029/2003GL017693

Mlynczak, M. G., Hunt, L. A., Russell, J. M. III, Marshall, B. T., Mertens, C. J., & Thompson, R. E. (2016). The global infrared energy budget of the thermosphere from 1947 to 2016 and implications for solar variability. *Geophysical Research Letters*, *43*, 11,934–11,940. https://doi.org/10.1002/2016GL070965

Mlynczak, M. G., Martin-Torres, F. J., Crowley, G., Kratz, D. P., Funke, B., Lu, G., et al. (2005). Energy transport in the thermosphere during the solar storms of April 2002. *Journal of Geophysical Research*, *110*, A12S25. https://doi.org/10.1029/2005JA011141

Nishioka, M., Tsugawa, T., Kubota, M., & Ishii, M. (2013). Concentric waves and short-period oscillations observed in the ionosphere after the 2013 Moore EF5 tornado. *Geophysical Research Letters*, *40*, 5581–5586. https://doi.org/10.1002/2013GL057963

Pradipta, R., Valladares, C. E., Carter, B. A., & Doherty, P. H. (2016). Interhemispheric propagation and interactions of auroral traveling ionospheric disturbances near the equator. *Journal of Geophysical Research: Space Physics*, *121*, 2462–2474. https://doi.org/10.1002/2015JA022043

Prölss, G. W., & Jung, M. J. (1978). Travelling atmospheric disturbances as a possible explanation for daytime positive storm effects of moderate duration at middle latitudes. *Journal of Atmospheric and Terrestrial Physics*, *40*(12), 1351–1354.

Redmon, R. J., Denig, W. F., Kilcommons, L. M., & Knipp, D. J. (2017). New DMSP database of precipitating auroral electrons and ions. *Journal of Geophysical Research: Space Physics*, *122*, 9056–9067. https://doi.org/10.1002/2016JA023339

Richmond, A. D., & Kamide, Y. (1988). Mapping electrodynamic features of the high-latitude ionosphere from localized observations: Technique. *Journal of Geophysical Research*, *93*(A6), 5741–5759. https://doi.org/10.1029/JA093iA06p05741

Ridley, A. J., Deng, Y., & Tóth, G. (2006). The global ionosphere-thermosphere model. *Journal of Atmospheric and Solar - Terrestrial Physics*, *68*(8), 839 864. https://doi.org/10.1016/j.jastp.2006.01.008

Roble, R. G., & Ridley, E. C. (1987). An auroral model for the NCAR thermospheric general circulation model (TGCM). *Annales Geophysicae Series A-upper Atmosphere and Space Sciences*, *5*, 369–382.

Saito, T., Ito, Y., Inazu, D., & Hino, R. (2011). Tsunami source of the 2011 Tohoku-Oki earthquake, Japan: Inversion analysis based on dispersive tsunami simulations. *Geophysical Research Letters*, *38*, L00G19. https://doi.org/10.1029/2011GL049089

Shults, K., Astafyeva, E., & Adourian, S. (2016). Ionospheric detection and localization of volcano eruptions on the example of the April 2015 Calbuco events. *Journal of Geophysical Research: Space Physics*, *121*, 10,303–10,315. https://doi.org/10.1002/2016JA023382

Sojka, J. J., David, M., Schunk, R. W., & Heelis, R. A. (2012). A modeling study of the longitudinal dependence of storm time midlatitude dayside total electron content enhancements. *Journal of Geophysical Research*, *117*, A02315. https://doi.org/10.1029/2011JA017000

Solomon, S. C., Barth, C. A., & Bailey, S. M. (1999). Auroral production of nitric oxide measured by the SNOE satellite. *Geophysical Research Letters*, *26*(9), 1259–1262. https://doi.org/10.1029/1999GL900235

Solomon, S. C., & Qian, L. (2005). Solar extreme-ultraviolet irradiance for general circulation models. *Journal of Geophysical Research*, *110*, A10306. https://doi.org/10.1029/2005JA011160

Tsugawa, T., Saito, A., Otsuka, Y., Nishioka, M., Maruyama, T., Kato, H., et al. (2011). Ionospheric disturbances detected by GPS total electron content observation after the 2011 off the Pacific coast of Tohoku Earthquake. *Earth, Planets and Space*, *63*, 875–879. https://doi.org/10.5047/eps.2011.06.035

Yonker, J. D. (2013). Contribution of the first electronically excited state of molecular nitrogen to thermospheric nitric oxide, Ph.D. dissertation

Zhang, S.-R., Erickson, P. J., Goncharenko, L. P., Coster, A. J., Rideout, W., & Vierinen, J. (2017). Ionospheric bow waves and perturbations induced by the 21 August 2017 solar eclipse. *Geophysical Research Letters*, *44*, 12,067–12,073. https://doi.org/10.1002/2017GL076054

Zhang, Y., Paxton, L. J., Kil, H., Meng, C.-I., Mende, S. B., Frey, H. U., & Immel, T. J. (2003). Negative ionospheric storms seen by the IMAGE FUV instrument. *Journal of Geophysical Research*, *108*(A9), 1343. https://doi.org/10.1029/2002JA009797

Zhou, X.-Y., Haerendel, G., Moen, J. I., Trondsen, E., Clausen, L., Strangeway, R. J., et al. (2017). Shock aurora: Field-aligned discrete structures moving along the dawnside oval. *Journal of Geophysical Research: Space Physics*, *122*, 3145–3162. https://doi.org/10.1002/2016JA022666